Macro-fiber composite-based tactors for haptic applications

Alain Boldini, John-Ross Rizzo, and Maurizio Porfiri, *Fellow, IEEE*

***Abstract*—Haptic technology is a critical component of human-computer interfaces. Traditional haptic actuators are often unable to provide the broad frequency range and latency that is required in many advanced applications. To address this problem, we propose a new type of tactor based on macro-fiber composites (MFCs), composites of piezoelectric fibers. We propose a physics-based model for the actuation of the tactors, calibrated and validated through experiments. As our tactors are intended for haptic applications, we consider the role of skin on their response, an aspect seldom analyzed in the literature. In our experiments, we simulate the presence of the skin with a rubber membrane in contact with the tactor, with varying pre-stretch, mimicking different indentations of the tactor on the skin. The MFC-based tactor can always generate vibration amplitudes higher than skin discrimination thresholds, over the range of frequencies of interest for haptics, with a latency much smaller than traditional actuators. We theoretically investigate the effect of the skin on tactor vibrations, highlighting the individual roles of skin stiffness and damping and their combined effect across a series of pre-stretches. Our tactor shows promise in haptic applications, including assistive technologies and real-time feedback systems for training, safety, and monitoring.**

***Index Terms*—Actuator, Haptics, Macro-fiber composite, Piezoelectric, Skin.**

I. Introduction

WEARABLE technologies have seen a steadily increased in real-world deployments over the last couple of decades [1]–[3]. From watches with sensors that support real-time health monitoring [4] to virtual reality (VR) headsets that simulate environments and activities [5], wearable devices have changed our daily lives and will extend their reach with the advent of the Internet of Things [6]. Within wearable technology, haptics offers a critical form of feedback to the end user [7], [8]. Smart watches can vibrate to inform the user about a call or message on their phone [9]; vibration of VR controllers help recreate real-world perceptions [10]; and vibration of customized feedback belts provide unique user-in-the-loop cueing about potential hazards or ineffective compensatory strategies [11], [12].

A. Boldini was with the Department of Mechanical and Aerospace Engineering and the Center for Urban Science and Progress, New York University Tandon School of Engineering, Brooklyn, NY, 11222 USA.

J.-R. Rizzo was with the Department of Rehabilitation Medicine and the Department of Neurology, New York University Grossman School of Medicine, New York, NY 10016, USA, and with the Department of Mechanical and Aerospace Engineering and the Department of Biomedical Engineering, New York University Tandon School of Engineering, Brooklyn, NY, 11222 USA.

M. Porfiri was with the Department of Mechanical and Aerospace Engineering, the Department of Biomedical Engineering, and the Center for Urban Science and Progress, New York University Tandon School of Engineering, Brooklyn, NY, 11222 USA. e-mail: mporfiri@nyu.edu.

This work was supported in part by the National Science Foundation through grants CNS-1952180 and ITE-2236097.

Manuscript received August xx, 2022.

Wearable haptic technology has been widely considered for sensory substitution and augmentation [13], [14]. Touch and vibrations can relay information about the environment to a user with sensory loss, be it permanent (visual or hearing impairment) or temporary (such as first responders in unknown or hostile environments). Haptics plays a major role in assistive technologies, as it is the fastest and most resilient way to convey low-level, urgent information to the user [15], [16].

Two main classes of actuators have been widely adopted in haptic technology: linear resonant actuators (LRAs) and eccentric rotating masses (ERMs) [17], [18]. In LRAs, a mass attached to a spring is repeatedly moved along an axis at a predetermined frequency, generating vibrations. These actuators show good performance in terms of efficiency and response time, but are limited by their frequency operating range, which is narrowly centered around their resonance frequency. On the other hand, ERMs generate vibrations via the rotation of an unbalanced mass, rotating at a fixed distance from the shaft of the motor. By modulating the rotational speed of the motor, these actuators can work over a relatively large frequency range compared to LRAs. However, the inertia of the mass hinders their latency. LRA and ERM limitations could be critical in haptic applications that require multi-frequency, composite feedback to relay complex information with low latency.

Other types of solutions have been proposed to address some of the limitations of these actuators. In particular, magnetically driven actuators that improve on classical LRAs include voice-coil motors and moving-magnet actuators [19]–[21]. While these designs significantly extend the bandwidth of LRAs up to $1\,\mathrm{kHz}$, actuators of size compatible to haptic applications do not perform well at low frequencies [20], [21]. The use of vibrations at very high frequencies, over about $200 - 250\,\mathrm{Hz}$, tend to be uncomfortable for users [22].

Among several solutions based on so-called smart materials [23], piezoelectric-based actuators constitute a potential solution to address these limitations [24], [25]. This class of actuators offers a great control authority, with a wide range of operating frequencies and low latency. In this case, vibrations are generated by the deformation of the active piezoelectric material, which displays electromechanical coupling [26]. By imposing a periodic voltage across the electrodes of the piezoelectric material, periodic vibrations are induced. The bandwidth of piezoelectric actuators span the entire frequency range of skin mechanoreceptors, including low frequencies sensed by Meissner corpuscles [27]. Actuators based on composites of piezoelectric materials, so-called macro-fiber composites (MFCs) [28]–[30], offer superior performance in terms of forces generated, deformations, and durability, as compared

to traditional piezoceramics used in laminated piezoelectric actuators [31]. As such, they constitute an excellent candidate for haptic applications.

Within the realm of assistive technologies for blind and low vision individuals, we recently realized a system that combines computer vision with a wearable haptic feedback device to support orientation and mobility (inclusive of obstacle avoidance), see Fig. 1 [11], [12]. In the system, the computer vision algorithm detects obstacles that are in the surroundings of the user, among several other functions/services. The wearable haptic feedback device, a belt with MFC-based discrete actuators disposed on a grid, provides vibrotactile stimulation on the end user's abdomen, relative to the position of the obstacles in an egocentric reference frame.

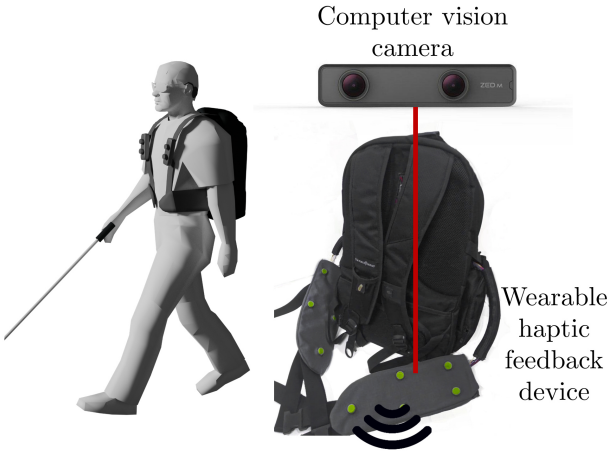

Fig. 1. Illustration of the wearable system we developed to assist blind and low vision individuals in navigation and obstacle avoidance. The system integrates a camera-based computer vision algorithm that identifies obstacles around the user and relays information about their position through haptic stimulation of the abdomen, via a vibrating belt with MFC-based discrete actuators.

We initially proposed a belt with four actuators on a 2×2 grid [32]. Actuation was generated by mounting MFCs in a buckled configuration, of which we exploited the nonlinear coupling between extension and out-of-plane displacement to generate vibrotactile stimulation. While these actuators showed promise in discrimination tests with human subjects, the displacements and forces generated were not sufficient to guarantee robust discrimination (feedback). Further, their use was limited to low frequencies.

Here, we propose a new tactor design based on MFCs. Our design leverages the advantages of piezoelectric-based actuators to develop a high-performance actuator for haptic applications, with a broad frequency range, low latency, tunable resonance frequency, and large vibration amplitude. For the design of the tactor, we focused on the frequency range in which skin mechanoreceptors are most sensitive, that is, below $250\,\mathrm{Hz}$ [33]. Within this frequency range, the discrimination threshold of skin is almost constant and equal to $50\,\mu\mathrm{m}$ on the abdomen [33], thereby setting as a reasonable design goal a tactor that could generate vibrations above $50\,\mu\mathrm{m}$ from few Hz up to $250\,\mathrm{Hz}$. This new type of tactor constitutes a significant improvement over previous MFC-based tactors, in terms of generated forces, displacements, and sturdiness. As the main field of application of the proposed tactors is haptic technology, we investigated the effect of the skin on tactor vibration. Compared to our previous studies [11], [34], this effort contributes: i) a physics-based theoretical model of tactor vibration; ii) an in-depth experimental characterization of the tactor across a range of independent experimental conditions that are designed for model calibration; and iii) a systematic investigation of the role of simulated skin on tactor vibration.

We put forward a theoretical model of the behavior of the tactor in contact with the skin. We derive exact solutions for the model in a few conditions, and establish a numerical method to study the vibration of the system in general. We then conduct a series of experiments on the tactor, towards calibrating and validating our model. Finally, we perform parametric analyses in which we systematically investigate the effect of the skin on tactor vibration. Specifically, we study the individual role of skin stiffness and damping on the frequency response of the tactor. Further, we assess their combined effect due to skin pre-stretch, which may vary due to tension introduced when wearing the haptic feedback device. These three analyses provide an overview of how skin affects the vibration of the tactor, an aspect that is not typically considered in the literature of actuators for haptic applications.

The rest of the paper is organized as follows. In Section II, we detail the design of our tactor. The mathematical model describing the actuation of the tactor is presented in Section III. Section IV introduces the calibration and validation of the theoretical model, including the experimental procedure, calibration process, and results. In Section V, we articulate a parametric analysis on the effect of simulated skin on vibration. Section VI concludes the manuscript, providing an overview of the main results of this work and directions of future research.

II. Description of the Tactor

The MFC in the tactor was comprised of a polymide/epoxy matrix, active piezoelectric fibers, and interdigitated electrodes (P1-type, Smart Material, FL, United States; Fig. 2(a)) [35]. We utilized M2814-P1 MFC actuators, with an active length of $28\,\mathrm{mm}$. Upon application of an external voltage, MFCs elongate axially due to the d_{33} piezoelectric effect. To generate bending deformations, we bonded the MFC to an aluminum backing plate with epoxy. The aluminum plate had size $52\,\mathrm{mm}$ (length) $\times$ $20\,\mathrm{mm}$ (width) $\times$ $0.25\,\mathrm{mm}$ (thickness). The aluminum plate had four holes at each corner to enable mounting with bolts. Upon clamping the aluminum plate, the elongation of the MFC would generate an out-of-plane bending displacement. Such an actuator differs substantially from our previous prototype in [32], where out-of-plane displacement was generated by the nonlinear coupling between extension and bending in a buckled configuration.

The MFC with the aluminum backing plate was fit in a custom 3D-printed case (Fig. 2b) made of polylactic acid

(PLA), which served several purposes: i) it supported the actuator and provided a sturdy structure on which the aluminum plate was clamped on both sides; ii) it protected the user from high voltage, necessary to drive the MFC; and iii) it helped amplify the vibration of the actuator. The overall case consisted of a bottom and a top part. The aluminum plate with the MFC was positioned inside the bottom part. The two parts were connected by four bolts that passed through the holes of the aluminum plate to create a fixed-fixed configuration. Four spacers of thickness $0.77\,\mathrm{mm}$ were used to avoid contact between the actuator and the case during actuation.

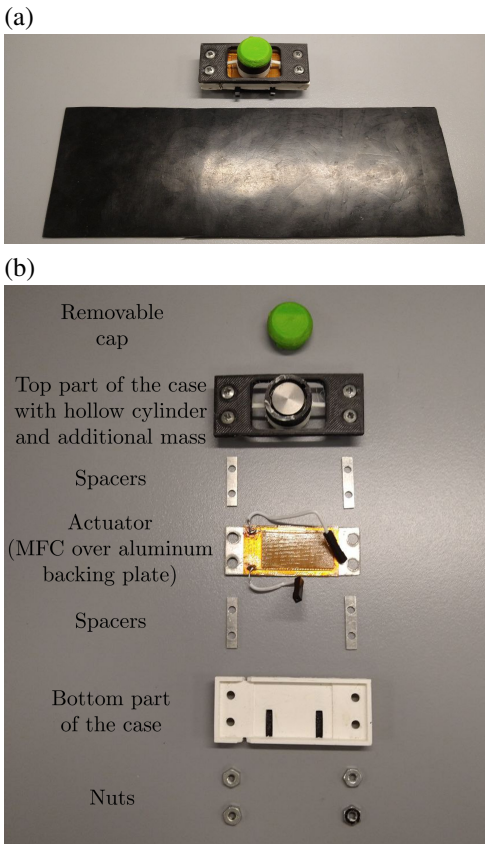

Fig. 2. Picture of a mounted tactor and of the membrane utilized in our experiments to simulate the skin (a); and explosion of a tactor (b).

The top part of the case included a large aperture that enabled transmission of the vibration from the actuator to the user, via a cylinder that was constrained by two flexible thermoplastic polyurethane (TPU) beams that sat on the MFC, which were pre-stressed during mounting. The bottom half of the cylinder is also printed in TPU, providing a deformable bottom surface that can maintain contact with the MFC during actuation. The top surface of the cylinder, in PLA, would be the only part of the tactor in contact with the skin of the user. We designed the $14\,\mathrm{mm}$-diameter cylinder to be hollow, with its top being removable via a thread that allowed for hosting an additional mass within the cylinder. Such a mass was utilized to tune the fundamental frequency of the tactor in the frequency range at which skin mechanoreceptors are most sensitive to vibrations (below $250\,\mathrm{Hz}$) [33]. To minimize the size of the cylinder, we utilized high-density tungsten and steel disks as additional masses, which were custom-made to fit the cylinder.

In our experiments, the cylinder was in contact with a commercial membrane made of rubber, mimicking the viscoelastic response of skin, with dimensions equal to $195\,\mathrm{mm}$ (length) $\times$ $66\,\mathrm{mm}$ (width) $\times$ $1.4\,\mathrm{mm}$ (thickness), mounted in a fixed-fixed position with free-length $170\,\mathrm{mm}$ (Fig. 2(a)). We recognize that a rubber membrane does not capture the complex mechanical behavior of real skin. We utilize this material to provide a simple viscoelastic response that displays the basic mechanical features of skin [36]–[38] and demonstrate that our model can capture their effect on tactors' vibrations, measured from experiments. We then conduct parametric analyses to understand the effect of more realistic values of skin stiffness and damping on the actuator.

The MFC was driven by a high-voltage amplifier (AMT2012-CE3, Smart Material, FL, United States), which linearly mapped the $[0, 2.5]\,\mathrm{V}$ range into $[-500, 0]\,\mathrm{V}$ and $[2.5, 5]\,\mathrm{V}$ range into $[0, 1500]\,\mathrm{V}$. In our experiments, the input to the high-voltage amplifier was provided by a function generator. When used in a wearable device, the input voltage can be provided by astable multivibrators, whose switching frequency can be tuned by a potentiometer driven by a microcontroller [11], [34].

III. Mathematical Model

Here, we establish a physics-based model for the tactor. We begin by presenting the governing equations of the system. We describe the different parameters of the model and detail how they were estimated (direct measurement, assumption from the literature, or experimental identification). We solve the governing equations for two static conditions, important for parameter identification. Finally, we present a numerical solution based on the Galerkin method to study vibrations. To improve readability, we have included a list of symbols in the Supplementary Material.

A. Governing equations

We model the tactor as a stepped beam [39] (Fig. 3(a)). We leverage the symmetry of the system to segment the actuator in three parts, with different properties and equations of motion in each of its section. The first segment is constituted by the aluminum plate only. The second segment comprises the aluminum beam and the MFC, assumed to be perfectly bonded to the aluminum plate. The third segment is is the one in contact with the cylinder. It is equal in composition to the second one, but its dynamics is governed by different equations, due to the mass in the cylinder, which adds to the linear mass, and the effect of the skin. For simplicity, we assume that the cylinder rigidly translates with the actuator during vibration, such that the viscoelastic forces generated by the skin are transmitted directly to the actuator in the form of symmetrically distributed stiffness and damping in the normal direction. We take inspiration from the literature on elastic foundations and employ a modified viscoelastic Winkler model to model the effect of the skin [40], [41]. Thus, the skin is considered as a distributed bed of springs and dampers with

coefficients k_s and c_s, respectively, connected to the third segment of the actuator, see Fig. 3b.

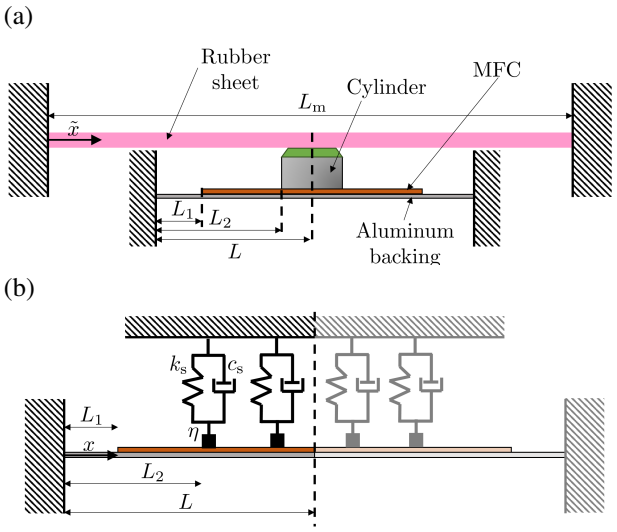

Fig. 3. (a) Schematics of the tactor, modeled as a symmetric stepped beam, in contact with the skin, modeled as a beam in contact with the cylinder of the tactor. (b) Viscoelastic Winkler model of the effect of the skin on the vibration of the actuator. Note that the cylinder is not bonded to the tactor. As the bottom of the cylinder is made of a flexible material (TPU), we expect the cylinder to adapt to the deformation of the MFC maintaining contact over all its bottom surface, as it is kept in contact by the stiffness of the skin and the two flexible beams attached to the case, pre-stressed during the mounting, see Fig. 2.

We consider a reference frame whose x-axis is aligned with the actuator axis and whose origin is on the left end of the actuator. The first segment is between $x = 0$ and $x = L_1$, the second segment between $x = L_1$ and $x = L_2$, and the third segment between $x = L_2$ and $x = L$, being L the semi-length of the actuator, see Fig. 3b. We use an index i to identify the segment to which properties refer to. For segment i, $w_i(x,t)$ is the transversal displacement, ρ_i is the linear density, and k_i is the bending stiffness.

The bending stiffness k_1 of the first segment of the actuator, constituted only by the aluminum plate, can be estimated from the standard formula $E_\mathrm{Al} I_\mathrm{Al}$. Here, E_Al is the Young modulus of aluminum and $I_\mathrm{Al} = b_\mathrm{Al} h_\mathrm{Al}^3/12$ is the moment of inertia of the aluminum plate's section, where b_Al and h_Al are the width and thickness of the aluminum plate, respectively.

The governing equation for the first two segments include the inertia, structural damping (assumed to be viscous with coefficient c_0), and elastic terms, such that[1]

$$\rho_i \ddot{w}_i + c_0 \dot{w}_i + k_i w_i'''' = 0, \tag{1}$$

with $i = 1, 2$. Here, a superimposed dot indicates partial derivative with respect to time, while a superscript prime is a partial derivative with respect to the x coordinate. For the last segment, we ought to account for the additional linear mass in the cylinder η and for the effect of the skin. Thus, we obtain

$$(\rho_3 + \eta)\ddot{w}_3 + c_0 \dot{w}_3 + k_3 w_3'''' = -k_\mathrm{s} w_3 - c_\mathrm{s} \dot{w}_3. \tag{2}$$

[1]Membrane stiffness is herein neglected, whereby in the considered conditions with small pre-stress its contribution was found to be negligible.

The parameters of the viscoelastic foundation are estimated by assimilating the skin to a fixed-fixed beam of free-length L_m, width b_m, and thickness h_m, made of a uniform material with Young modulus E_m (Fig. 3(b)). We opt for a one-dimensional model of the skin rather than a two-dimensional one, such as a membrane theory. In fact, we are not concerned with the most accurate representation of the deformation of the membrane, but rather to its effects on vibrations of the actuator along its first few modes. Should one be interested in high-frequency behavior, it may be warranted to include two-dimensional dynamics, toward capturing out-of-plane bending and torsional modes.

The parameter k_s captures both skin bending stiffness and geometric stiffness due to a pre-stretch δ. To estimate k_s, we compute the displacement due to a concentrated force at the center. A pointwise stiffness is obtained by dividing the concentrated force by the mid-span displacement. We convert such a concentrated stiffness into a distributed one by scaling over the segment $L - L_2$. The concentrated and distributed stiffness generate the same elastic force on the tactor when the third segment of the tactor (on which the distributed stiffness acts) translates uniformly. Details on the derivation of k_s can be found in the Supplementary Information.

The governing equations are supplemented by a series of boundary and interface conditions [42]. At the left end of the actuator, we consider a fixed boundary condition, such that

$$w_1(0,t) = 0, \tag{3a}$$

$$w_1'(0,t) = 0. \tag{3b}$$

In the middle of the actuator, we apply symmetric boundary conditions,

$$w_3'(L,t) = 0, \tag{4a}$$

$$k_3 w_3'''(L,t) = \frac{F_\mathrm{app}(t)}{2}, \tag{4b}$$

where we considered the possibility that a concentrated load $F_\mathrm{app}(t)$ is applied at the center of the actuator. At the interfaces, we impose the continuity of transversal displacement, section rotation, bending moment, and transversal force. At $x = L_1$, we have a jump in the properties of the beam, as well as a concentrated bending moment due to the piezoelectric effect, such that

$$w_1(L_1,t) = w_2(L_1,t), \tag{5a}$$

$$w_1'(L_1,t) = w_2'(L_1,t), \tag{5b}$$

$$k_1 w_1''(L_1,t) = k_2 w_2''(L_1,t) - \mu V(t), \tag{5c}$$

$$k_1 w_1'''(L_1,t) = k_2 w_2'''(L_1,t), \tag{5d}$$

where μ is the piezoelectric voltage-moment coefficient relating voltage and bending moment, while $V(t)$ is the voltage applied across the MFCs' electrodes. At the second interface, we have no jump in the beam properties, such that

$$w_2(L_2,t) = w_3(L_2,t), \tag{6a}$$

$$w_2'(L_2,t) = w_3'(L_2,t), \tag{6b}$$

$$w_2''(L_2,t) = w_3''(L_2,t), \tag{6c}$$

$$w_2'''(L_2,t) = w_3'''(L_2,t). \tag{6d}$$

As we only perform static or modal analysis, we consider homogeneous initial conditions.

B. Model parameters

Our model contains several parameters that have been calibrated through measurements (direct or indirect) or determined from the literature (Table I). Measures and experiments were performed both on the tactor and rubber membrane that we utilized to simulate skin.

TABLE I
MODEL PARAMETERS.

Parameter	Value	Source
L	$2.2 \times 10^{-2}\,\mathrm{m}$	Directly measured
L_1	$0.8 \times 10^{-2}\,\mathrm{m}$	Directly measured
L_2	$1.5 \times 10^{-2}\,\mathrm{m}$	Directly measured
b_{Al}	$2.0 \times 10^{-2}\,\mathrm{m}$	Directly measured
h_{Al}	$2.0 \times 10^{-4}\,\mathrm{m}$	Directly measured
L_{m}	$1.7 \times 10^{-1}\,\mathrm{m}$	Directly measured
b_{m}	$6.6 \times 10^{-2}\,\mathrm{m}$	Directly measured
h_{m}	$1.4 \times 10^{-3}\,\mathrm{m}$	Directly measured
ρ_1	$1.13 \times 10^{-2}\,\mathrm{kg/m}$	Directly measured
$\rho_2 = \rho_3$	$2.50 \times 10^{-2}\,\mathrm{kg/m}$	Directly measured
E_{Al}	$69\,\mathrm{GPa}$	Assumed from the literature [43]
$k_2 = k_3$	$7.0 \times 10^{-3}\,\mathrm{N\,m^2}$	Identified from static deflection under an external mechanical loading and change in resonance due to additional mass
μ	$-1.33 \times 10^{-5}\,\mathrm{N\,m/V}$	Identified from static deflection under an applied voltage
c_0	$159\,\mathrm{kg/(m\,s)}$	Identified from response to harmonic applied voltage without membrane
c_{s}^{δ}	$5.48 \times 10^{4}\,\mathrm{kg/(m\,s)}$	Identified from response to harmonic applied voltage with membrane
c_{s}^{0}	$165\,\mathrm{kg/(m\,s)}$	Identified from response to harmonic applied voltage with membrane
E_{m}	$6.95\,\mathrm{MPa}$	Identified from static deflection of the membrane under gravity (see Supplementary Information)

Geometric dimensions of the tactor and rubber membrane were measured with a ruler (L, L_1, L_2, b_{Al}, L_{m}, b_{m}) or a digital caliper (h_{Al}, h_{m}), depending on needed resolution. We obtained the linear masses ρ_1 and $\rho_2 = \rho_3$ of the three segments by measuring the mass of the aluminum beam and the MFC, and then dividing them by their lengths. While in principle the additional linear mass η varies with x, we neglect such a variation by assuming that it is distributed over a rectangular cuboid rather than a cylinder. Thus, we estimated it by taking the ratio between the mass added in the cylinder and the length of the third segment, $L - L_2$.

The only parameter that has been assumed from the literature is the Young modulus of aluminum, E_{Al}. All the remaining parameters have been identified from experiments. We obtained the bending stiffness $k_2 = k_3$ of the second and third segment of the actuator from the static deflection of the tactor under the external mechanical loading and the change in its fundamental frequency due to the additional mass. Further, we estimated the piezoelectric voltage-moment coefficient μ of the actuator from the static deflection of the tactor under a voltage imposed across the MFC electrodes. From the frequency response of the freely vibrating tactor to a harmonic applied voltage, we retrieved the structural damping coefficient c_0. The same experiment with the tactor vibrating in contact with the membrane was utilized to estimate the skin damping coefficient c_s. We assumed that skin damping may depend on the pre-stretch δ of the membrane, $c_{\mathrm{s}} = c_{\mathrm{s}}(\delta)$. As such, we utilized the same procedure used for the identification of c_0 to identify $c_{\mathrm{s}}(\delta)$ for each value of δ. From the *a posteriori* analysis of the identified values of $c_{\mathrm{s}}(\delta)$, we discovered an almost linear dependence of c_{s} on δ. Thus, we employed a linear approximation $c_{\mathrm{s}}(\delta) = c_{\mathrm{s}}^{\delta}\delta + c_{\mathrm{s}}^{0}$ to extrapolate the damping coefficient of the skin to levels of pre-stretch δ not studied in our experiments. Finally, we conducted an experiment on the membrane to infer its Young modulus E_{m}, by measuring its deformation under gravity. All the experiments on the tactor are described in Section IV, and the experiment on the membrane is detailed in the Supplementary Information.

C. Exact solutions

We put forward two exact solutions for the static deflections of the tactor, used for model calibration on experimental data.

1) Static deflection under an external mechanical loading: The theoretical static deflection under an external mechanical loading F_{app} at its center, in the absence of skin ($k_{\mathrm{s}} = 0$ and $c_{\mathrm{s}} = 0$) and with shorted electrodes ($V = 0$), was computed exactly from Eqs. (1), (2), (5), and (6) as

$$\begin{aligned} w_{\mathrm{th}}^{F} = F_{\mathrm{app}}[&k_1^2(L-L_1)^4 + k_2^2 L_1^4 \\ &- 2k_1k_2L_1(-2L^3 + 3L^2L_1 - 2LL_1^2 + L_1^3)] \\ &/\{24k_1^2[k_1(L-L_1) + k_2L_1]\}. \end{aligned} \tag{7}$$

2) Static deflection under an applied voltage: The theoretical static deflection under an imposed voltage V across the electrodes, in the absence of skin ($k_{\mathrm{s}} = 0$ and $c_{\mathrm{s}} = 0$) and external loading ($F_{\mathrm{app}} = 0$), was computed exactly from Eqs. (1), (2), (5), and (6) as

$$w_{\mathrm{th}}^{V} = \frac{LL_1(L_1 - L)}{2[k_1(L-L_1) + k_2L_1]}\mu V. \tag{8}$$

D. Numerical solution

General analytical solutions of the equations of motion in Eqs. (1) and (2) are challenging to establish. As such, we adopt a Galerkin approach to determine the solution of the equations

of motion [44]. We write a weak form of Eqs. (1) and (2) and sum them to obtain a problem over the entire domain $[0, L]$,

$$\begin{aligned}&\int_0^{L_1} \delta w_1 \rho_1 \ddot{w}_1 \,\mathrm{d}x + \int_{L_1}^{L_2} \delta w_2 \rho_2 \ddot{w}_2 \,\mathrm{d}x \\ &+ \int_{L_2}^{L} \delta w_3 (\rho_3 + \eta) \ddot{w}_3 \,\mathrm{d}x + \int_0^{L_1} \delta w_1 c_0 \dot{w}_1 \,\mathrm{d}x \\ &+ \int_{L_1}^{L_2} \delta w_2 c_0 \dot{w}_2 \,\mathrm{d}x + \int_{L_2}^{L} \delta w_3 c_0 \dot{w}_3 \,\mathrm{d}x + \int_0^{L_1} \delta w_1 k_1 w_1'''' \,\mathrm{d}x \\ &+ \int_{L_1}^{L_2} \delta w_2 k_2 w_2'''' \,\mathrm{d}x + \int_{L_2}^{L} \delta w_3 k_3 w_3'''' \,\mathrm{d}x \\ &+ \int_{L_2}^{L} \delta w_3 k_\mathrm{s} w_3 \,\mathrm{d}x + \int_{L_2}^{L} \delta w_3 c_\mathrm{s} \dot{w}_3 \,\mathrm{d}x = 0.\end{aligned} \tag{9}$$

Here, δw_i is an arbitrary variation defined over the i-th segment. By applying twice integration by parts over the bending stiffness terms in Eq. (9), employing boundary conditions and interface conditions in Eqs. (3), (4), (5), and (6), and setting $F_\mathrm{app} = 0$ as no external loading is present during vibrations, we find

$$\begin{aligned}&\int_0^{L_1} \delta w_1 \rho_1 \ddot{w}_1 \,\mathrm{d}x + \int_{L_1}^{L_2} \delta w_2 \rho_2 \ddot{w}_2 \,\mathrm{d}x \\ &+ \int_{L_2}^{L} \delta w_3 (\rho_3 + \eta) \ddot{w}_3 \,\mathrm{d}x + \int_0^{L_1} \delta w_1 c_0 \dot{w}_1 \,\mathrm{d}x \\ &+ \int_{L_1}^{L_2} \delta w_2 c_0 \dot{w}_2 \,\mathrm{d}x + \int_{L_2}^{L} \delta w_3 c_0 \dot{w}_3 \,\mathrm{d}x + \int_0^{L_1} \delta w_1'' k_1 w_1'' \,\mathrm{d}x \\ &+ \int_{L_1}^{L_2} \delta w_2'' k_2 w_2'' \,\mathrm{d}x + \int_{L_2}^{L} \delta w_3'' k_3 w_3'' \,\mathrm{d}x + \int_{L_2}^{L} \delta w_3 k_\mathrm{s} w_3 \,\mathrm{d}x \\ &+ \int_{L_2}^{L} \delta w_3 c_\mathrm{s} \dot{w}_3 \,\mathrm{d}x = -\delta w_1'(L_1) \mu V.\end{aligned} \tag{10}$$

We define global variables over the entire semi-length of the actuator by stitching together the piecewise-defined functions,

$$w(x,t) = \begin{cases} w_1(x,t) & \text{for } 0 \le x < L_1, \\ w_2(x,t) & \text{for } L_1 \le x < L_2, \\ w_3(x,t) & \text{for } L_2 \le x \le L. \end{cases}, \tag{11a}$$

$$\delta w(x,t) = \begin{cases} \delta w_1(x,t) & \text{for } 0 \le x < L_1, \\ \delta w_2(x,t) & \text{for } L_1 \le x < L_2, \\ \delta w_3(x,t) & \text{for } L_2 \le x \le L. \end{cases}. \tag{11b}$$

We project such global variables on the same set of shape functions $N_j(x)$, $j = 1, \ldots, \infty$, such that

$$w(x,t) = \sum_{j=1}^{\infty} N_j(x) q_j(t), \tag{12a}$$

$$\delta w(x,t) = \sum_{j=1}^{\infty} N_j(x) \delta q_j(t), \tag{12b}$$

where $q_j(t)$ and $\delta q_j(t)$ are the generalized coordinates and their arbitrary variations, respectively.

By substituting Eq. (12) into Eq. (10), truncating the sum to a finite number of terms n, and considering the arbitrariness in the variations $\delta q_j(t)$, we obtain

$$\mathbf{M}\ddot{\mathbf{q}} + \mathbf{C}\dot{\mathbf{q}} + \mathbf{K}\mathbf{q} = \mathbf{B}V(t), \tag{13}$$

where $\mathbf{q}(t) = \begin{bmatrix} q_1(t) & \ldots & q_n(t) \end{bmatrix}^\mathrm{T}$ is a vector collating all generalized coordinates and

$$\begin{aligned}\mathbf{M} = \rho_1 \int_0^{L_1} \mathbf{N}\mathbf{N}^\mathrm{T} \,\mathrm{d}x + \rho_2 \int_{L_1}^{L_2} \mathbf{N}\mathbf{N}^\mathrm{T} \,\mathrm{d}x \\ + (\rho_3 + \eta) \int_{L_2}^{L} \mathbf{N}\mathbf{N}^\mathrm{T} \,\mathrm{d}x,\end{aligned} \tag{14a}$$

$$\mathbf{C} = c_0 \int_0^{L} \mathbf{N}\mathbf{N}^\mathrm{T} \,\mathrm{d}x + c_\mathrm{s} \int_{L_2}^{L} \mathbf{N}\mathbf{N}^\mathrm{T} \,\mathrm{d}x, \tag{14b}$$

$$\begin{aligned}\mathbf{K} = k_1 \int_0^{L_1} \mathbf{N}''\mathbf{N}''T \,\mathrm{d}x + k_2 \int_{L_1}^{L_2} \mathbf{N}''\mathbf{N}''T \,\mathrm{d}x \\ + k_3 \int_{L_2}^{L} \mathbf{N}''\mathbf{N}''T \,\mathrm{d}x + k_\mathrm{s} \int_{L_2}^{L} \mathbf{N}\mathbf{N}^\mathrm{T} \,\mathrm{d}x,\end{aligned} \tag{14c}$$

$$\mathbf{B} = -\mathbf{N}'(L_1)\mu, \tag{14d}$$

being $\mathbf{N}(x) = \begin{bmatrix} N_1(x) & \ldots & N_n(x) \end{bmatrix}^\mathrm{T}$ a vector that collects all the shape functions.

1) Selection of the shape functions: Shape functions in Eq. (12) should form a complete basis and satisfy Dirichlet boundary conditions in Eqs. (3), (4), (5), and (6) [44]. We use the symmetric mode-shapes of a double cantilever beam with length $2L$ [39],

$$\begin{aligned}\phi_j(x,t) = &\cos(\beta_j x) - \cosh(\beta_j x) \\ &- \frac{\cos(2\beta_j L) - \cosh(2\beta_j L)}{\sin(2\beta_j L) - \sinh(2\beta_j L)} \left[\sin(\beta_j x) - \sinh(\beta_j x)\right],\end{aligned} \tag{15}$$

where $\beta_j L$ satisfies the transcendental equation $\cos(2\beta_j L)\cosh(2\beta_j L) - 1 = 0$.

Due to the presence of discontinuities in the beam, concentrated bending moments, and additional forces generated by the skin, we consider two supplementary shape functions that help improve the convergence of the numerical solution [42]:

- the static response of a uniform beam to a concentrated bending moment at $x = L_1$,

$$\tilde{\phi}_1(x) = \begin{cases} (L - L_1)x^2 & \text{for } 0 \le x < L_1, \\ L_1(-x^2 + 2Lx - L_1 L) & \text{for } L_1 \le x \le L \end{cases}; \tag{16}$$

- the static response of a uniform beam to a uniform distributed force over $[L_2, L]$,

$$\tilde{\phi}_2(x) = \begin{cases} 4(L_2 - L)x^3 + \left(4L^2 - 6L_2^2 + 2\frac{L_2^3}{L}\right)x^2 \\ \quad \text{for } 0 \le x < L_2, \\ x^4 - 4Lx^3 + \left(4L^2 + 2\frac{L_2^3}{L}\right)x^2 - 4L_2^3 x + L_2^4 \\ \quad \text{for } L_2 \le x \le L \end{cases}. \tag{17}$$

By incorporating these additional shape functions, we define the vector of shape functions as $\mathbf{N}(x) = \begin{bmatrix} \phi_1(x), \ldots, \phi_{n-2}(x), \tilde{\phi}_1(x), \tilde{\phi}_2(x) \end{bmatrix}^\mathrm{T}$, for $n \ge 3$.

Through convergence analysis, we found that five mode-shapes, in addition to the two supplementary shape functions, are enough to provide a good approximation of our results. Thus, we utilize a total of $n = 7$ shape functions.

IV. Model Calibration and Validation

We performed a series of experiments with the aim of calibrating the parameters of the tactor. These experiments included the static deflection of the tactor under an external mechanical loading, change in the fundamental frequency due to additional mass in the cylinder, static deflection of the tactor under an imposed voltage across the MFC electrodes, and the frequency response to a harmonic applied voltage, without and with contact with the skin (simulated by a rubber membrane). The frequency response to a harmonic applied voltage was also utilized as a validation for our model.

Below, we detail the experimental procedure, calibration process, and results for each of these experiments.

1) Static deflection under an external mechanical loading & change in resonance due to additional mass: To provide an estimate of the bending stiffness $k_2 = k_3$ of the second and third segment of the actuator, we performed a static loading test and investigated the change in the tactor fundamental frequency due to an additional mass in the cylinder. In the static loading test [34], we applied known weights at the center of the actuator and measured its deflection at the same point through a laser displacement sensor. To avoid issues with slacks in the actuator mount, an offset of $10\,\mathrm{g}$ was initially applied to the actuator. We utilized five weights in addition to the offset, tested in a random order: 20, 50, 100, 200, and $500\,\mathrm{g}$. We zeroed the laser displacement sensor after releasing each of the loads, to avoid hysteretic effects. During these experiments, the electrodes of the MFC were shorted. We recognize that MFCs have a different modulus in compression and extension and that the actuator is not symmetric with respect to its mid-axis. As such, we conducted the experiment in two configurations, one with the loads applied on the MFC side and one on the aluminum plate side. For each configuration, we repeated the measurements ten times.

We also studied the change in the tactor fundamental frequency due to the addition of mass in the cylinder, mounted on top of the actuator. We identified the resonance frequency with different masses in the cylinder through frequency voltage sweeps. We applied linear voltage sweeps from 25 to $525\,\mathrm{Hz}$ for a duration of $300\,\mathrm{s}$ with peak-to-peak amplitude of $5\,\mathrm{V}$, while measuring the displacement at the center of the tactor with a laser displacement sensor. The signal from the laser displacement sensor was sampled at $5,000\,\mathrm{Hz}$ with a 16-bit data acquisition system (National Instrument 6341), without any pre-conditioning. The mass was applied by hot gluing the 3D printed cylinder over the actuator and fixing it with duct tape to ensure a stable positioning. Modeling clay, inserted in the cylinder, was utilized to increase the additional mass after each voltage sweep. We utilized additional masses from $1.75\,\mathrm{g}$ to $9.75\,\mathrm{g}$, with steps of $1\,\mathrm{g}$. To reduce the effect of noise, we filtered the displacement time-series with the `lowpass` function in Matlab®, with a cut-off frequency at $600\,\mathrm{Hz}$. From the filtered time-series, we identified the resonance frequency as the peak of the Fourier transform of the output between $125\,\mathrm{Hz}$ and $500\,\mathrm{Hz}$, which were selected to remove spurious peaks in the frequency response.

We utilized the static and vibratory data to estimate $k_2 = k_3$. As a first approximation, we neglected the change in stiffness depending on the MFC being in tension and compression by averaging the experimental results on static deflection obtained from loading on the MFC and the aluminum sides. The theoretical static deflection under the external mechanical loading was obtained from Eq. (7). For the change in fundamental frequency due to the additional mass, we utilized an estimate from our numerical solution in Eq. (13). Specifically, assuming low damping, we set $\mathbf{C} \approx \mathbf{0}$, and we also consider $V(t) = 0$. We hypothesized a solution in the form $\mathbf{q}(t) = \mathbf{q}_0 e^{\mathrm{i}\omega t}$, where i is the imaginary unit, and we identified the fundamental angular frequency as the lowest generalized eigenvalue ω of the problem $(-\omega^2\mathbf{M} + \mathbf{K})\mathbf{q}_0 = \mathbf{0}$.

We estimated the bending stiffness $k_2 = k_3$ by minimizing the weighted sum of the distance between the theoretical and experimental static deflection under an external mechanical loading and the distance between the theoretical and experimental fundamental frequencies with varying additional mass. From this procedure, we found $k_2 = k_3 = 7.0 \times 10^{-3}\,\mathrm{N\,m^2}$. Such a value enabled an excellent reconstruction of both the deflection at the center of the actuator due to the application of an external mechanical load (Fig. 4) and the resonance frequency of the tactor with varying additional mass (Fig. 5).

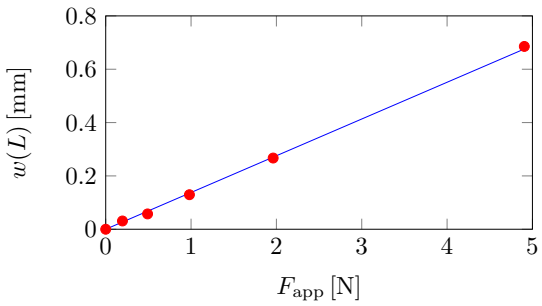

Fig. 4. Comparison between the theoretical (solid blue) and experimental (red dots) displacement $w(L)$ at the center of the actuator, for a known weight F_{app} applied at the same point.

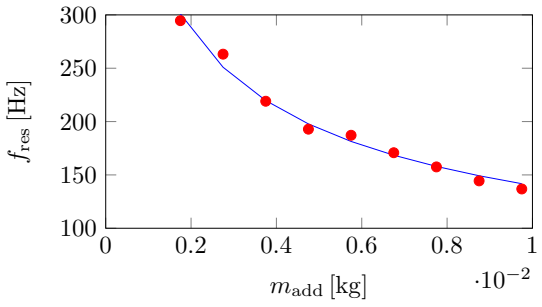

Fig. 5. Comparison between the theoretical (solid blue) and experimental (red dots) fundamental frequency f_{res}, for different masses m_{add} added in the cylinder of the tactor.

2) Static deflection under an applied voltage: We identified the piezoelectric voltage-moment coefficient μ through the static response of the actuator to an imposed voltage [34]. Specifically, we applied known, constant voltages across the MFC electrodes and measured the displacement at the center of the actuator through a laser displacement sensor. We applied voltage levels between 0.5 and 5 V, generated by a voltage supplier, with steps of 0.5 V. The HVA linearly converted the $[0, 2.5]$ V input voltage range into the output range $[-0.5, 0]$ kV, and the $[2.5, 5]$ V input range into $[0, 1.5]$ kV. In our experiments, we zeroed the laser displacement sensor at 2.5 V (corresponding to an effective zero output voltage), and measured the deflection with respect to this configuration for different levels of the applied voltage to account for hysteretic effects. We repeated each measurement five times.

We estimated μ as the value that minimized the difference between theoretical deflection from Eq. (8) and experimental results on the static deflection under an applied voltage – upon using k_2 estimated from experiments 1). We obtained a value for the piezoelectric voltage-moment coefficient of $\mu = -1.33 \times 10^{-5}\,\mathrm{N\,m/V}$. Such a parameter leads to an excellent agreement between theoretical and experimental results (Fig. 6).

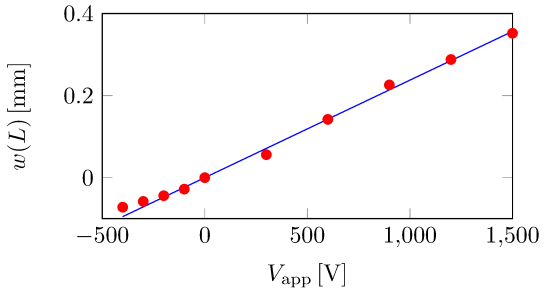

Fig. 6. Comparison between the theoretical (solid blue) and experimental (red dots) displacement $w(L)$ at the center of the actuator, for a known voltage V_{app} applied across the MFC electrodes.

3) Response to harmonic applied voltage: We studied the frequency response of the tactor to a harmonic voltage and reconstructed the frequency-displacement curve for a fixed value of the mass. To avoid hysteresis in the piezoelectric response of the MFC, we fixed the frequency of the input voltage, set to 5 V amplitude, and we measured the displacement of the center of the tactor. We selected the following frequencies: 25, 50, 75, 100, 125, 150, 155, 160, 165, 170, 175, 180, 185, 190, 195, 200, 225, and 250 Hz. We computed the amplitude of the response at each frequency as the difference between the maximum and the minimum of each displacement time-series.

We identified the structural damping coefficient c_0 from the frequency response, for a set value of the mass. We selected the structural damping coefficient minimizing the difference between the amplitudes of the fundamental resonance peaks from the experiment and from our theoretical model. To estimate the theoretical amplitude, in Eq. (13) we set a harmonic input voltage $V = V_0 e^{\mathrm{i}\omega t}$ with amplitude V_0 and angular frequency ω, and computed the output assuming that it is harmonic with the same angular frequency. Stiffness and piezoelectric coupling were set to the values determined from experiments 1) and 2). Although we utilized a mass of 11 g in the experiments, we identified a theoretical mass of 7.73 g by matching the theoretical and experimental fundamental frequencies. Such a discrepancy is likely associated with a sub-optimal fixing of the additional mass. We found that $c_0 = 159\,\mathrm{kg/(m\,s)}$ provides the best reconstruction of the peak in the frequency response (Fig. 9(a)).

We repeated the same experiments with the tactor in contact with a membrane, simulating the skin (Fig. 7). To proxy different levels of indentation of the tactor in the skin, we applied different pre-stretches to the membrane. To this end, we fixed one end of the membrane and applied elongations ΔL_{m} of 0, 0.05, 0.10, 0.15, 0.20, and 0.25 in (0, 1.27, 2.54, 3.81, 5.08, and 6.35 mm). For each displacement, we repeated the same procedure as for the frequency response in the absence of membrane, measuring the displacement at the center of the tactor (on the skin side) at the same frequencies.

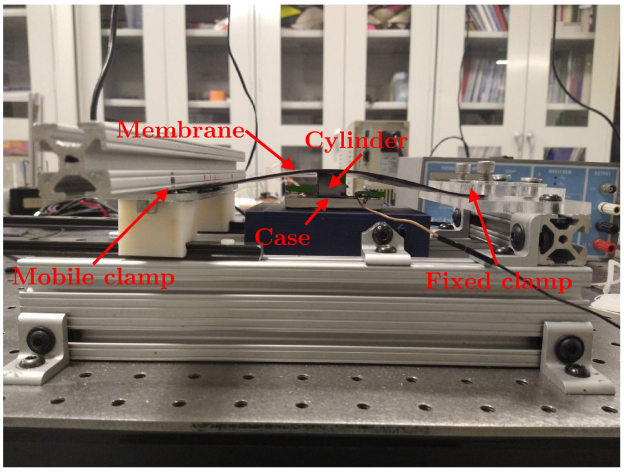

Fig. 7. Experimental setup illustrating the tactor in contact with the membrane during the vibration tests.

From these experiments, we proceeded to identify the damping associated with the skin, assuming a dependence on the pre-stretch $\delta = \Delta L_{\mathrm{m}}/L_{\mathrm{m}}$. Following the same procedure as for structural damping, we minimized the difference in the theoretical and experimental peak amplitude between 100 and 250 Hz. We fitted the corresponding curve $c_{\mathrm{s}}(\delta)$ with a line, $c_{\mathrm{s}}(\delta) = c_{\mathrm{s}}^{\delta}\delta + c_{\mathrm{s}}^{0}$, with fixed intercept c_{s}^{0} equal to the identified value $c_{\mathrm{s}}(0) = 165\,\mathrm{kg/(m\,s)}$ (Fig. 8). We obtained a good fit with $R^2 = 0.86$, indicating that, at least in the range of damping considered in our experiments, damping varied linearly with δ, with a slope $c_{\mathrm{s}}^{\delta} = 5.48 \times 10^4\,\mathrm{kg/(m\,s)}$.

Figure 9 compares the theoretical frequency response against the tactor experimental frequency response, used to validate our model; as for damping identification, we utilized an additional mass of 7.73 g in the theoretical computations. Theoretical and experimental responses were highly correlated for all cases in Fig. 9 (Pearson correlation coefficient $r > 0.8$ for all, with $p < 10^{-4}$). For the free vibration of the tactor not in contact with the membrane (Fig. 9(a)), we observed a sharp resonance in the experimental response around 160 Hz, corresponding to the tactor fundamental frequency. Vibrations

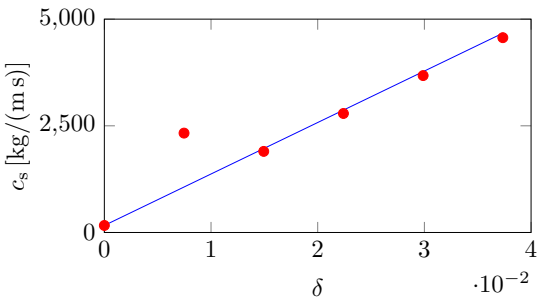

Fig. 8. Experimentally identified values of c_s as a function of the pre-stretch δ of the membrane (red dots), along with the linear fit with an intercept equal to the identified value of $c_s(0)$ (blue line).

at resonance had a considerably higher amplitude (almost twice) than at low frequencies. Our theoretical response was in close agreement with experimental observations, with a few differences. First, the theoretical response overestimated the amplitude at low frequencies. Second, it displayed a zero in the response before the resonance peak, absent in the experimental response. Finally, the resonance peak in the theoretical response was more spread than in the experiments.

By placing the tactor in contact with the unstretched membrane, we did not register any change in the experimental response at low frequencies (Fig. 9(b)). At resonance, we recorded a considerable decrease in the vibration amplitude compared to free vibrations of the tactor. This decrease was more prominent at the resonance frequency, as the amplitude decreases of almost a three-fold factor. Interestingly, the fundamental frequency increased by about 15 Hz compared to the case without membrane. Our simulations followed a similar trend, predicting a remarkable decrease of the vibration amplitude at resonance and an increase of the resonance frequency. We also noticed a slight increase in the amplitude at low frequencies, not reflected in the experiment. The zero in the frequency response was shifted towards higher frequencies compared to the case without membrane.

Increasing the pre-stretch of the membrane considerably affected the experimental frequency response of the tactor (Fig. 9(c)), as resonance is completely suppressed and the frequency response becomes almost flat, with slightly higher values at low frequencies. Further increasing the pre-stretch caused small variations in the response of the tactor, with an overall small decrease in the amplitude (Fig. 9(d-f)). Our theoretical response closely matched experimental observations. Interestingly, the zero in the response is no more present. For small pre-stretches (Fig. 9(c)), we found higher amplitudes at low frequency than at high frequency. For higher pre-stretches (Fig. 9(d-f)), we registered a decrease in the amplitude at low frequency and a decrease at high frequency, such that the frequency response became substantially flat.

V. Parametric Analyses

Once we validated the theoretical model, we performed a series of parametric analyses to unravel the role of the skin on tactor vibrations, using the numerical solution in Eq. (13).

A. Effect of skin stiffness

First, we considered the individual effect of the stiffness of the skin on the vibration of the tactor. We set the damping due to the skin to zero and computed the frequency response of the actuator for varying Young moduli E_m of the membrane, for a fixed 1 mm applied elongations (equivalent to 0.6% pre-stretch). We selected the following values that span the variability of skin stiffness [45]: 10^3, 10^6, 10^7, 10^8, and 10^9 Pa. Results of the parametric analysis are in Fig. 10.

By considering a small value of the stiffness of the skin (10^3 Pa), we obtained a similar response to the free vibration of the tactor in Fig. 9(a). Increasing the stiffness four orders of magnitudes affected the actuation minimally. We started to observe changes in the frequency response by raising the Young modulus to 10^7 Pa. In this case, we registered a small increase in the vibration amplitude at low frequencies, along with a slight shift towards higher frequencies of the zero of the response and resonance. At resonance, we noticed a small decrease in the peak amplitude. By increasing the Young modulus to 10^8 Pa, we found an analogous shift of the zero and resonance, along with a decrease of the peak amplitude. Further, we registered a decrease in the amplitude at low frequencies. For the highest stiffness of 10^9 Pa, the response of the tactor changed drastically. Resonance was completely suppressed, resulting in an almost flat response, with a small increase in amplitude towards higher frequencies.

B. Effect of skin damping

Second, we considered the individual effect of the stiffness of the skin on the vibration of the tactor. We set the pre-stretch of the membrane to zero and the Young modulus of the membrane to 6.95×10^6 Pa. We then computed the frequency response of the actuator by varying the damping coefficient c_s of the skin. We considered a characteristic damping coefficient $\bar{c} = k_1 \tau / L^4 \approx 6.66\,\mathrm{kg/(m\,s)}$, being $\tau = \sqrt{\rho_1/(k_1 L^4)} \approx 1.7$ ms the characteristic time scale, and we simulated the frequency response of the tactor for $10^{-3}\,\bar{c}$, $\bar{c}$, $10\,\bar{c}$, $25\,\bar{c}$, and $50\,\bar{c}$. Results of this analysis are in Fig. 11.

A small damping coefficient $10^{-3}\,\bar{c}$ did not significantly affect the tactor response, which is dominated by the structural damping. By increasing the damping to $\bar{c}$, we observed modest variations in the response. The largest effect was noted at resonance, as the peak amplitude became slightly lower. Increasing the damping of an order of magnitude elicited a considerable reduction in the peak amplitude at resonance, along with a small decrease in the amplitude at low frequency and a shift to higher frequencies of the zero. Setting damping to $25\,\bar{c}$ and $50\,\bar{c}$ caused noticeable reductions in the amplitude at frequencies higher than the fundamental frequency.

C. Effect of skin pre-stretch

Finally, we investigated the effect of pre-stretch of the skin on the vibration of the tactor. As tactors would be mounted on adjustable straps or belts, such a parametric analysis was meant to describe the effect of different levels of mounting tensions. Variations in the skin pre-stretch would affect both stiffness

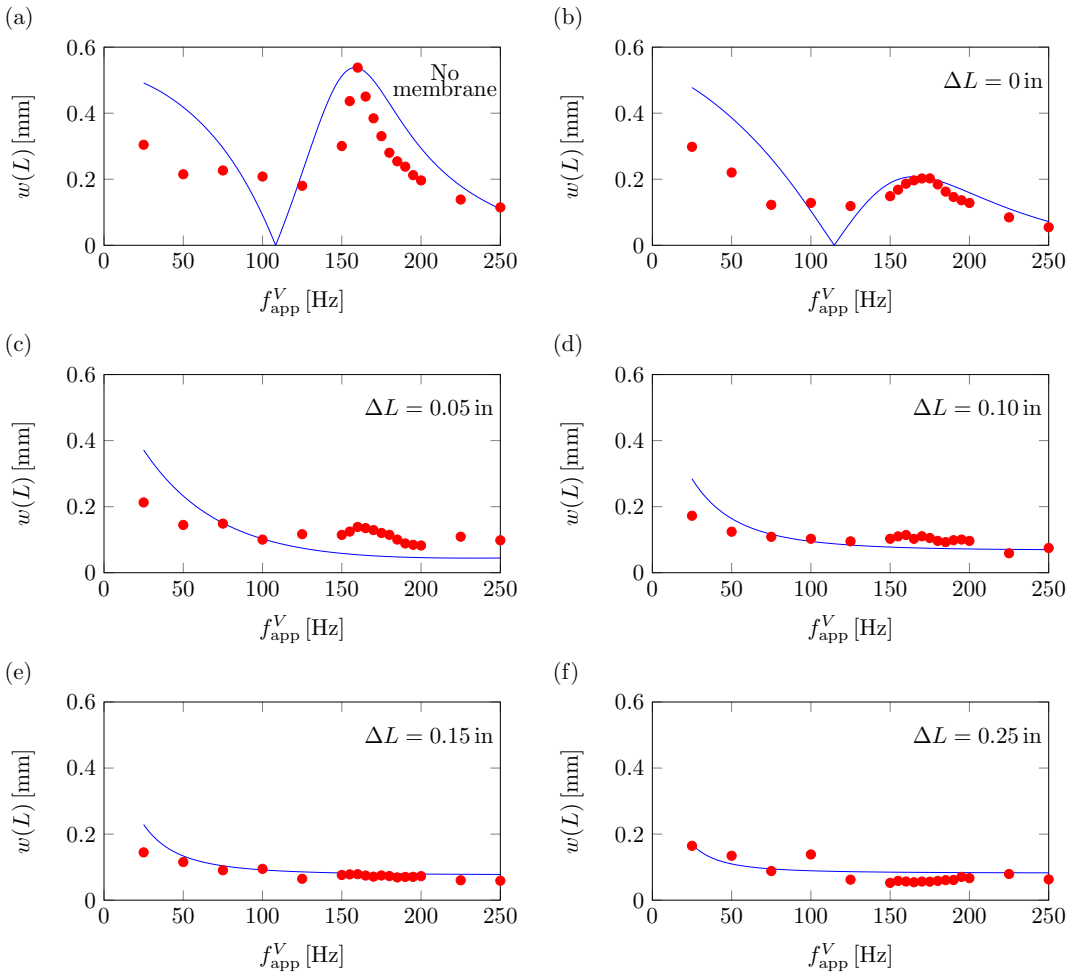

Fig. 9. Theoretical (blue solid line) and experimental (red dots) frequency responses of the tactor vibrating freely (a) or in contact with the skin (b-f), for different values of the pre-stretch of the rubber membrane, corresponding to elongations ΔL_{m} of 0 in (0 mm) (b), 0.05 in (1.27 mm) (c), 0.10 in (2.54 mm) (d), 0.15 in (3.81 mm) (e), and 0.25 in (6.35 mm) (f). f^V_{app} is the frequency of the imposed sinusoidal voltage with fixed 5 V amplitude, and $w(L)$ is the displacement at the center of the tactor. For the cases in contact with the membrane, k_{s} and c_{s} vary in the ranges $[4.1, 8.5 \times 10^4]\,\text{kg}/(\text{m}\,\text{s}^2)$ and $[165, 2212]\,\text{kg}/(\text{m}\,\text{s})$, respectively.

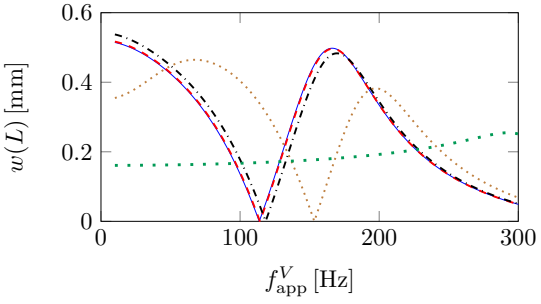

Fig. 10. Theoretical frequency responses of the tactor for different values of the stiffness of the skin. f^V_{app} is the frequency of the imposed sinusoidal voltage with fixed 5 V amplitude, and $w(L)$ is the displacement at the center of the tactor. Blue solid, red dashed, black dash-dotted, brown finely dotted, and green loosely dotted curves represent the response of the tactor in contact with the membrane, with Young moduli of 10^3, 10^6, 10^7, 10^8, and 10^9 Pa, respectively.

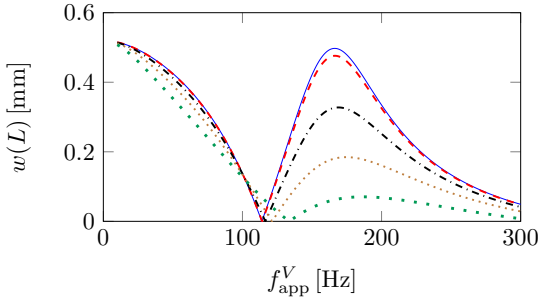

Fig. 11. Theoretical frequency responses of the tactor for different values of the damping of the skin. f^V_{app} is the frequency of the imposed sinusoidal voltage with fixed 5 V amplitude, and $w(L)$ is the displacement at the center of the tactor. Blue solid, red dashed, black dash-dotted, brown finely dotted, and green loosely dotted curves represent the response of the tactor in contact with the membrane, with damping coefficients of $10^{-3}\,\bar{c}$, $\bar{c}$, $10\,\bar{c}$, $25\,\bar{c}$, and $50\,\bar{c}$, respectively.

(due to the geometric stiffness contribution) and damping (due to the dependence of damping on the pre-stretch, see Fig. 8). As for damping, we set the Young modulus of the membrane to 6.95×10^6 Pa and we considered a linear variation of the

damping coefficient with the pre-stretch δ of the skin, with the parameters identified from the experiments on the rubber membrane. We then studied the frequency response of the membrane for different values of the pre-stretch: 10^{-5}, 10^{-4}, 10^{-3}, 10^{-2}, and 10^{-1}. Higher values of pre-stretch are likely to be uncomfortable for the user wearing the haptic device. Results of this parametric analysis are displayed in Fig. 12.

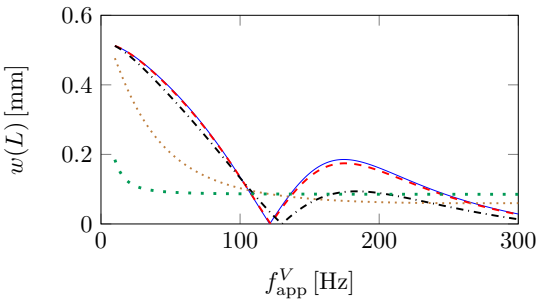

Fig. 12. Theoretical frequency responses of the tactor for different values of the pre-stretch of the skin. f^V_{app} is the frequency of the imposed sinusoidal voltage with fixed 5 V amplitude, and $w(L)$ is the displacement at the center of the tactor. Blue solid, red dashed, black dash-dotted, brown finely dotted, and green loosely dotted curves represent the response of the tactor in contact with the membrane, with pre-stretch of 10^{-5}, 10^{-4}, 10^{-3}, 10^{-2}, and 10^{-1}, respectively.

Small values of the pre-stretch, in the order of $10^{-3} - 10^{-2}$ % yielded frequency responses similar to the unstretched membrane case in Fig. 9(b). Increasing the pre-stretch to 0.1 % caused considerable effects only at resonance, with a decrease in the peak amplitude. Elsewhere, we noted only a slight reduction in the amplitude, along with a shift to higher frequencies of the zero of the response. When the pre-stretch reached 1%, we registered a completely different response of the actuator. Specifically, the vibration amplitude started from values similar to the unstretched case at low frequencies, and it decreased monotonically until 200 Hz, plateauing to an almost constant value. In addition, the zero of the frequency response disappears. Interestingly, by increasing the pre-stretch of another order of magnitude, we recovered an almost flat response, with only a sharp variation at low frequencies. While at low frequencies the vibration amplitude was much smaller than in any other case, the constant value at which the response plateaued was larger than the one for a 1 % pre-stretch.

VI. Discussion and Conclusions

Haptic technology is attracting increasing interest within the engineering community for its use in human-computer interactions across aviation [46], medicine [47], mobile devices [48], robotics [49], and VR [50]. Motivated by applications in assistive technologies that require broad frequency ranges and low latencies, not afforded by standard tactors, we proposed a new type of MFC-based actuator. These composites of piezoelectric materials can generate large displacements and forces over a broad range of frequencies, with a fast response due to their electromechanical transduction and low inertia. We leveraged these advantages to build a new MFC-based tactor, which includes an MFC bonded to an aluminum plate and mounted in a 3D-printed case. The case was designed to protect users from the high voltages required for actuation, improve tactor performance, and tune its fundamental frequency. Modulation of the resonance frequency was afforded by the addition of a controlled mass to the hollow cylinder tethered to the mount, which transmits the vibration to the skin of the user. We tuned the resonance frequency in the stimulation range at which skin is most sensitive, below 250 Hz.

We put forward a physics-based model to describe the mechanical behavior of the tactor. Importantly, we accounted for the effects of skin on the vibration of the tactor, as if in its ecologically valid application state. Such an aspect, which is of critical importance for haptic applications [47], has been seldom considered in the literature with regards to haptic actuation. To include the effect of the skin in a tractable way, we took inspiration from the theory of elastic and viscoelastic foundations, which are at the heart of geotechnical and civil engineering. We modeled the effect of the skin on the tactor as that of a bed of springs and dampers, whose parameters were estimated from theoretical arguments and experiments.

Our theoretical analysis was complemented by a series of experiments that were utilized to calibrate the parameters of our model and validate its results. In vibration experiments, we simulated the presence of the skin through a rubber membrane in contact with the tactor. To mimic different tensions of the skin at which a wearable with tactors may be worn, we tested a series of membrane pre-stretches. We showed that our model can adequately predict the frequency response of the actuator and the effect that the skin has on it. Regardless of the pre-stretch of the membrane, our experimental results demonstrated that the tactors can generate vibrations with amplitude over 50 μm, which is the physiological discrimination threshold over the abdomen for frequencies below 250 Hz [33].

Once validated, we exploited the theoretical model to systematically investigate the effect of the skin on tactor dynamics, through a series of parametric analyses. We considered the individual influence of skin stiffness and damping on the tactor frequency response, and their combined effect due to a change in skin pre-stretch. To unravel the role of skin stiffness on tactor vibration, we varied the Young modulus of the skin over seven order of magnitudes, corresponding to the identified stiffness of skin from different experiments in the literature [45]. Tactor response was marginally affected by the elastic response of the skin for five orders of magnitude. Only at stiffness values of 10^8 Pa we found an effect of skin stiffness, in terms of an appreciable increase in the fundamental frequency and a moderate reduction of the amplitude at resonance. For even higher values of the stiffness, the vibration amplitude of the tactor became substantially independent of the frequency. We further studied the effect of skin damping by varying the damping coefficient as a multiple of the characteristic damping coefficient. For values of damping below such a value, we found a negligible influence of the viscous response of the skin on the tactor. Increasing the value of damping over this value caused a sharp decrease in the amplitude of the response at resonance. Finally, we investigated the effect of pre-stretch of the membrane on the frequency response of the tactor, from 10^{-3}% to 10%. Variations of the pre-stretch led to an intricate change in the skin stiffness and damping. Overall, the

effect of pre-stretch became important at around 0.1%, where we registered a decrease in the amplitude of the response at resonance. Further stretching the membrane caused severe changes: at 1% resonance was suppressed and at 10% the response was practically constant.

Our work is not free of limitations that should be addressed in future efforts. From the point of view of the actuator design, further improvements can be pursued in the cylinder attachment. The length of the TPU beams and their pattern could be modified to optimize the balance between flexibility, to avoid excessive reduction in the vibration amplitude, and vertical force on the tactor, to ensure that the mass in the cylinder effectively contributes to reducing the resonance frequency. From the modeling perspective, while our work considered the effect of the skin, its physics has been considerably simplified. Skin is a nonlinear, multilayer, anisotropic soft tissue, with damping dependent on stimulation frequency [51], [52]. Here, we adopted a semi-empirical approach to model the effect of the skin on the dynamics of the tactor. Future endeavors should consider physics-based models of skin, potentially extending previous waterbed models of skin mechanics [53] or continuum-based viscoelastic foundation models, such as Vlasov's [54].

Further, we put forward some hypotheses that may not be verified in general conditions, such as the fact that the surface of the cylinder in contact with the actuator does not vary during the vibration and the cylinder translates rigidly with the actuator: while the satisfactory results of our model support the plausibility of these assumptions, approaches based on finite element and multibody simulations may be pursued to corroborate these claims. We also assume that skin only provides a normal, symmetrical force on the actuator, not accounting for shear and off-center effects occurring in realistic conditions. With respect to the experiments, we utilized a rubber membrane to simulate the effect of the skin. We envision further experiments with materials that more closely resemble the mechanical properties of skin than rubber, such as hydrogels [55]. While our tactors outperform our previous MFC-based prototypes [32], which proved promising in discrimination tests with human subjects, we anticipate the need to perform analogous tests. Despite these limitations, our work constitutes a meaningful advancement in high-performance actuators for haptic applications in medicine and beyond.

REFERENCES

[1] J. McCann and D. Bryson, *Smart clothes and wearable technology*. Elsevier, 2009.

[2] E. Sazonov, *Wearable Sensors: Fundamentals, implementation and applications*. Academic Press, 2020.

[3] T. Page, "A forecast of the adoption of wearable technology," *International Journal of Technology Diffusion (IJTD)*, vol. 6, no. 2, pp. 12–29, 2015.

[4] M. Wu and J. Luo, "Wearable technology applications in healthcare: a literature review," *Online Journal of Nursing Informatics*, vol. 23, no. 3, 2019.

[5] W. Barfield, *Fundamentals of wearable computers and augmented reality*. CRC press, 2015.

[6] H. Raad, *Fundamentals of IoT and Wearable Technology Design*. John Wiley & Sons, 2020.

[7] L. Jones, *Haptics*. MIT Press, 2018.

[8] B. Hannaford and A. M. Okamura, "Haptics," in *Springer Handbook of Robotics*. Springer, 2016, pp. 1063–1084.

[9] C. Seim, R. Pontes, S. Kadiveti, Z. Adamjee, A. Cochran, T. Aveni, P. Presti, and T. Starner, "Towards haptic learning on a smartwatch," in *Proceedings of the 2018 ACM International Symposium on Wearable Computers*, 2018, pp. 228–229.

[10] M. A. Srinivasan and C. Basdogan, "Haptics in virtual environments: Taxonomy, research status, and challenges," *Computers & Graphics*, vol. 21, no. 4, pp. 393–404, 1997.

[11] A. Boldini, A. L. Garcia, M. Sorrentino, M. Beheshti, O. Ogedegbe, Y. Fang, M. Porfiri, and J.-R. Rizzo, "An inconspicuous, integrated electronic travel aid for visual impairment," *ASME Letters in Dynamic Systems and Control*, vol. 1, no. 4, 2021.

[12] Z. Yuan, T. Azzino, Y. Hao, Y. Lyu, H. Pei, A. Boldini, M. Mezzavilla, M. Beheshti, M. Porfiri, T. E. Hudson, W. Seiple, Y. Fang, S. Rangan, Y. Wang, and J.-R. Rizzo, "Network-aware 5G edge computing for object detection: Augmenting wearables to "see" more, farther and faster," *IEEE Access*, vol. 10, pp. 29 612–29 632, 2022.

[13] D. T. Pawluk, R. J. Adams, and R. Kitada, "Designing haptic assistive technology for individuals who are blind or visually impaired," *IEEE Transactions on Haptics*, vol. 8, no. 3, pp. 258–278, 2015.

[14] P. Bach-y Rita and S. W. Kercel, "Sensory substitution and the human–machine interface," *Trends in Cognitive Sciences*, vol. 7, no. 12, pp. 541–546, 2003.

[15] K. E. MacLean, "Designing with haptic feedback," in *Proceedings of the 2000 IEEE International Conference on Robotics and Automation (ICRA)*, vol. 1. IEEE, 2000, pp. 783–788.

[16] F. Danieau, A. Lécuyer, P. Guillotel, J. Fleureau, N. Mollet, and M. Christie, "Enhancing audiovisual experience with haptic feedback: a survey on HAV," *IEEE Transactions on Haptics*, vol. 6, no. 2, pp. 193–205, 2012.

[17] J. R. Blum, P. E. Fortin, F. Al Taha, P. Alirezaee, M. Demers, A. Weill-Duflos, and J. R. Cooperstock, "Getting your hands dirty outside the lab: A practical primer for conducting wearable vibrotactile haptics research," *IEEE Transactions on Haptics*, vol. 12, no. 3, pp. 232–246, 2019.

[18] H. Huang, T. Li, C. Antfolk, C. Enz, J. Justiz, and V. M. Koch, "Experiment and investigation of two types of vibrotactile devices," in *2016 6th IEEE International Conference on Biomedical Robotics and Biomechatronics (BioRob)*. Ieee, 2016, pp. 1266–1271.

[19] E. J. Shahoian, "Moving magnet actuator for providing haptic feedback," Jan. 3 2006, uS Patent 6,982,696.

[20] W. McMahan and K. J. Kuchenbecker, "Dynamic modeling and control of voice-coil actuators for high-fidelity display of haptic vibrations," in *2014 IEEE Haptics Symposium (HAPTICS)*. IEEE, 2014, pp. 115–122.

[21] TactileLabs, "Haptuator Mark II," http://tactilelabs.com/wp-content/uploads/2012/07/TL002-09-A_v1.01.pdf, last Accessed 18 February 2023.

[22] K. Myles and J. T. Kalb, "An evaluation of signal annoyance for a head-mounted tactile display," Army Research Lab, Tech. Rep., 2015.

[23] X. Xie, S. Liu, C. Yang, Z. Yang, T. Liu, J. Xu, C. Zhang, and X. Zhai, "A review of smart materials in tactile actuators for information delivery," *C - Journal of Carbon Research*, vol. 3, no. 4, p. 38, 2017.

[24] Y. Chen, Y. Yang, M. Li, E. Chen, W. Mu, R. Fisher, and R. Yin, "Wearable actuators: An overview," *Textiles*, vol. 1, no. 2, pp. 283–321, 2021.

[25] S. Biswas and Y. Visell, "Emerging material technologies for haptics," *Advanced Materials Technologies*, vol. 4, no. 4, p. 1900042, 2019.

[26] A. Arnau, *Piezoelectric transducers and applications*. Springer, 2004, vol. 2004.

[27] Y. Li and A. S. Wong, *Clothing biosensory engineering*. Woodhead Publishing, 2006.

[28] O. Bilgen, A. Erturk, and D. J. Inman, "Analytical and experimental characterization of macro-fiber composite actuated thin clamped-free unimorph benders," *Journal of Vibration and Acoustics*, vol. 132, no. 5, 2010.

[29] S. Shahab and A. Erturk, "Coupling of experimentally validated electroelastic dynamics and mixing rules formulation for macro-fiber composite piezoelectric structures," *Journal of Intelligent Material Systems and Structures*, vol. 28, no. 12, pp. 1575–1588, 2017.

[30] A. Erturk and D. J. Inman, *Piezoelectric energy harvesting*. John Wiley & Sons, 2011.

[31] H. A. Sodano, G. Park, and D. J. Inman, "An investigation into the performance of macro-fiber composites for sensing and structural vibration applications," *Mechanical Systems and Signal Processing*, vol. 18, no. 3, pp. 683–697, 2004.

[32] P. Phamduy, J.-R. Rizzo, T. E. Hudson, M. Torre, K. Levon, and M. Porfiri, "Communicating through touch: Macro fiber composites for

tactile stimulation on the abdomen," *IEEE Transactions on Haptics*, vol. 11, no. 2, pp. 174–184, 2018.
[33] R. W. Cholewiak, J. C. Brill, and A. Schwab, "Vibrotactile localization on the abdomen: Effects of place and space," *Perception & Psychophysics*, vol. 66, no. 6, pp. 970–987, 2004.
[34] A. Boldini, J.-R. Rizzo, and M. Porfiri, "A piezoelectric-based advanced wearable: obstacle avoidance for the visually impaired built into a backpack," in *Nano-, Bio-, Info-Tech Sensors, and 3D Systems IV*, vol. 11378. SPIE, 2020, p. 1137806.
[35] Smart Material, "Macro fiber composite," https://www.smart-material.com/media/Datasheets/MFC_V2.4-datasheet-web.pdf, last Accessed 25 July 2022.
[36] M. Christensen, C. Hargens III, S. Nacht, and E. Gans, "Viscoelastic properties of intact human skin: instrumentation, hydration effects, and the contribution of the stratum corneum," *Journal of Investigative Dermatology*, vol. 69, no. 3, pp. 282–286, 1977.
[37] J. Pereira, J. Mansour, and B. Davis, "Dynamic measurement of the viscoelastic properties of skin," *Journal of Biomechanics*, vol. 24, no. 2, pp. 157–162, 1991.
[38] F. H. Silver, J. W. Freeman, and D. DeVore, "Viscoelastic properties of human skin and processed dermis," *Skin Research and Technology*, vol. 7, no. 1, pp. 18–23, 2001.
[39] S. S. Rao, *Vibration of continuous systems*. John Wiley & Sons, 2019.
[40] A. D. Kerr, "Elastic and viscoelastic foundation models," *Journal of Applied Mechanics*, vol. 31, no. 3, pp. 491–498, 1964.
[41] D. A. Dillard, B. Mukherjee, P. Karnal, R. C. Batra, and J. Frechette, "A review of Winkler's foundation and its profound influence on adhesion and soft matter applications," *Soft Matter*, vol. 14, no. 19, pp. 3669–3683, 2018.
[42] C. Maurini, M. Porfiri, and J. Pouget, "Numerical methods for modal analysis of stepped piezoelectric beams," *Journal of sound and vibration*, vol. 298, no. 4-5, pp. 918–933, 2006.
[43] D. B. Marghitu, *Mechanical engineer's handbook*. Elsevier, 2001.
[44] L. Meirovitch, *Fundamentals of vibrations*. Waveland Press, 2010.
[45] H. K. Graham, J. C. McConnell, G. Limbert, and M. J. Sherratt, "How stiff is skin?" *Experimental Dermatology*, vol. 28, pp. 4–9, 2019.
[46] D. Van Baelen, M. van Paassen, J. Ellerbroek, D. A. Abbink, and M. Mulder, "Flying by feeling: Communicating flight envelope protection through haptic feedback," *International Journal of Human–Computer Interaction*, vol. 37, no. 7, pp. 655–665, 2021.
[47] A. M. Okamura, C. Basdogan, S. Baillie, and W. S. Harwin, "Haptics in medicine and clinical skill acquisition," *IEEE Transactions on Haptics*, vol. 4, no. 3, pp. 153–154, 2011.
[48] A. Chang and C. O'Sullivan, "Audio-haptic feedback in mobile phones," in *CHI'05 Extended Abstracts on Human Factors in Computing Systems*, 2005, pp. 1264–1267.
[49] O. Khatib, O. Brock, K.-S. Chang, D. Ruspini, L. Sentis, and S. Viji, "Human-centered robotics and interactive haptic simulation," *The International Journal of Robotics Research*, vol. 23, no. 2, pp. 167–178, 2004.
[50] W. Dangxiao, G. Yuan, L. Shiyi, Y. Zhang, X. Weiliang, and X. Jing, "Haptic display for virtual reality: progress and challenges," *Virtual Reality & Intelligent Hardware*, vol. 1, no. 2, pp. 136–162, 2019.
[51] H. Joodaki and M. B. Panzer, "Skin mechanical properties and modeling: A review," *Proceedings of the Institution of Mechanical Engineers, Part H: Journal of Engineering in Medicine*, vol. 232, no. 4, pp. 323–343, 2018.
[52] R. O. Potts, D. A. Chrisman Jr, and E. M. Buras Jr, "The dynamic mechanical properties of human skin *in vivo*," *Journal of Biomechanics*, vol. 16, no. 6, pp. 365–372, 1983.
[53] M. Srinivasan and K. Dandekar, "An investigation of the mechanics of tactile sense using two-dimensional models of the primate fingertip," *Journal of Biomechanical Engineering*, vol. 118, no. 1, pp. 48–55, 1996.
[54] R. Jones and J. Xenophontos, "The Vlasov foundation model," *International Journal of Mechanical Sciences*, vol. 19, no. 6, pp. 317–323, 1977.
[55] R. Fu, L. Tu, Y. Zhou, L. Fan, F. Zhang, Z. Wang, J. Xing, D. Chen, C. Deng, G. Tan *et al.*, "A tough and self-powered hydrogel for artificial skin," *Chemistry of Materials*, vol. 31, no. 23, pp. 9850–9860, 2019.

Alain Boldini received B.Sc. degree in Aerospace Engineering and M.Sc. degree in Aeronautical Engineering from Politecnico di Milano, Milan, Italy, in 2015 and 2017, respectively, M.Sc. in Aerospace Engineering from Politecnico di Torino, Turin, Italy, in 2018, and Ph.D. in Mechanical Engineering from New York University Tandon School of Engineering in 2022. He is a Postdoctoral Associate and Adjunct Professor at the New York University Tandon School of Engineering. He is involved in research in smart advanced materials, assistive technologies, and dynamical systems.

John-Ross (JR) Rizzo received his medical degree from New York Medical College, Alpha Omega Alpha Honors, on academic scholarship. He is currently a physician-scientist at NYU Langone Medical Center's Rusk Rehabilitation, where he serves as vice chair of Innovation and Equity for Physical Medicine and Rehabilitation with cross-appointments in the Department of Neurology and the Departments of Biomedical & Mechanical and Aerospace Engineering at NYU-Tandon School of Engineering. He is also the Associate Director of Healthcare for the NYU Wireless Laboratory in the Department of Electrical and Computer Engineering at NYU-Tandon. He leads the Visuomotor Integration Laboratory (VMIL) and the REACTIV Laboratory (Rehabilitation Engineering Alliance and Center Transforming Low Vision), where his team focuses on assistive technology for blind and low vision individuals and benefits from his own personal experiences with vision loss. He is the author of 10 book chapters, more than 80 peer-reviewed articles and many poster presentations. His research interests lie within the realm of neurorehabilitation, assistive technologies, and health equity. Dr. Rizzo was awarded the prestigious Crain's 40 under 40 award in New York Business for his medical devices, including his wearable technology. He has also been featured in several lay articles and also featured in videos and press releases. In 2018, he was a highlighted speaker in NYU's TEDx "Re-Vision" Series. He is a member of American Medical Association, American College of Physicians, American Academy of PM&R (AAPM&R), Association of Academic Physiatry (AAP), and American Heart Association.

Maurizio Porfiri (Fellow, IEEE) is an Institute Professor at New York University Tandon School of Engineering, with appointments in the Center for Urban Science and Progress, the Department of Mechanical and Aerospace Engineering, and the Department of Biomedical Engineering. He received M.Sc. and Ph.D. degrees in Engineering Mechanics from Virginia Tech, in 2000 and 2006; a "Laurea" in Electrical Engineering (with honors) and a Ph.D. in Theoretical and Applied Mechanics from the University of Rome "La Sapienza" and the University of Toulon (dual degree program), in 2001 and 2005, respectively. He is the director of the Dynamical Systems Laboratory, where he conducts and supervises research on complex systems, with applications from mechanics to behavior, public health, and robotics. Maurizio Porfiri is the author of approximately 400 journal publications and the recipient of the National Science Foundation CAREER award. He has been included in the "Brilliant 10" list of Popular Science and his research featured in major media outlets, including CNN, NPR, Scientific American, and Discovery Channel. Other significant recognitions include the elevation to both ASME and IEEE; invitations to the Frontiers of Engineering Symposium and the Japan-America Frontiers of Engineering Symposium organized by the National Academy of Engineering; invitations to the third and fourth World Laureate Forums; the Outstanding Young Alumnus award by the college of Engineering of Virginia Tech; the ASME Gary Anderson Early Achievement Award; the ASME DSCD Young Investigator Award; the ASME C.D. Mote, Jr. Early Career Award; and the Research Excellence Award at New York University.